

# The impact of spring-neap tidal-stream cycles in tidal energy assessments in the Chilean Inland Sea



Osvaldo Artal <sup>a, b, \*</sup>, Oscar Pizarro <sup>c, d, e</sup>, Héctor H. Sepúlveda <sup>c</sup>

<sup>a</sup> Doctoral Program in Physics, University of Concepción, Barrio Universitario s/n, Casilla 160-C, Concepción, Chile

<sup>b</sup> Environmental Department, Aquaculture Research Division, Fisheries Development Institute (IFOP), Camino a Tenten S/N, Castro, Chile

<sup>c</sup> Department of Geophysics, University of Concepción, Concepción, Chile

<sup>d</sup> COPAS Sur-Austral, University of Concepción, Concepción, Chile

<sup>e</sup> Millennium Institute of Oceanography (IMO), University of Concepción, Concepción, Chile

## ARTICLE INFO

### Article history:

Received 9 February 2018

Received in revised form

7 February 2019

Accepted 16 February 2019

Available online 22 February 2019

### Keywords:

Tidal-stream energy

Spring tides

Neap tides

CROCO

Chilean inland sea

## ABSTRACT

The Chilean Inland Sea (CIS) has natural conditions for marine tidal energy development. Recent studies show that lunar variability in the tides should be considered, because the practical power generation varies considerably when large differences exist between spring and neap tides. Using a high resolution (~1 km) 2D depth-averaged numerical model, we investigate the effect of lunar cycle variability in the CIS and this impact on tidal energy evaluation by validating a 30 days simulation. There are two highly energetic areas where currents exceed 2 m/s 50% of the time: the Chacao and Desertores Channels. Both zones are dominated by semi-diurnal tides, and tidal current amplitude shows large changes during spring and neap tides. Due to these changes power density can vary considerably in a period of 2 weeks. In the Chacao Channel, tidal-stream power is four times as large during spring tide ( $40 \text{ kW/m}^2$ ) compared to neap tide ( $10 \text{ kW/m}^2$ ). Tidal-stream power is only significant during spring tide in the Desertores Channel ( $8 \text{ kW/m}^2$ ). This work is a contribution to understanding the tidally driven flows in an inland sea and the importance of considering the variations between spring and neap tides in tidal-stream energy assessment.

© 2019 Elsevier Ltd. All rights reserved.

## 1. Introduction

Chile has large potential renewable energy sources such as wind, geothermal, wave and tidal energy [1]. In 2013, government legislation set a goal of 20% non-conventional renewable energy (NCRE) generation by 2025. This goal is within reach, since NCRE generation was already 15% of total power capacity in 2016 [2]. Most of the recent developments have been achieved with solar energy, which constituted 76% of NCRE production in 2017. Other alternatives sources are wind [3], small-hydroelectricity generation [4], and geothermal energy [5]. It is surprising then that, with over 4000 km ocean coastline, marine renewable energies have not played a bigger role in the energy matrix.

The predictable nature of tidal energy makes it an attractive source of renewable energy to explore. Characterizing and defining

sites for deploying available technologies are important steps for evaluating tidal energy use. Tidal characteristics of most coastal locations have been studied with a perspective toward navigation safety. Tidal dynamic depend on both the global characteristics of the tide and regional and local geometry, which can lead to tidal resonance [6], or flow constriction.

Direct measurements have been used to characterize tidal currents. Existing technology allows the deployment of bottom-based Acoustic Doppler Current Profilers (ADCP) for 1–3 months. Tidal energy assessments in Chile were done by Garrad Hassan Consulting in 2009 [7]. Their assessment included a study of several factors, such as environmental restrictions, areas with depths greater than 50 m, marine protected areas, and distances to the national electricity grid, which were weighted to rank different zones. The Chilean Inland Sea (CIS) with the Chacao Channel and the Corcovado Gulf, as well as the Straits of Magellan were zones with high tidal-energy potential that were highlighted in the report [7].

Mean spring peak current ( $V_{msp}$ ) has been used as an indicator of tidal energy resource. However, in areas with a large neap/spring variability, this indicator can lead to an incorrect representation of

\* Corresponding author. Environmental Department, Aquaculture Research Division, Fisheries Development Institute (IFOP), Camino a Tenten S/N, Castro, Chile.  
E-mail address: [osvaldo.artal@ifop.cl](mailto:osvaldo.artal@ifop.cl) (O. Artal).

the energy resource [8,9]. Maps of root mean cubed velocity are also used for power density estimation [10,11]. This methodology requires a modeled velocity well represented, because the power density is a function of cubed velocity and therefore the errors in the power density prediction are higher than the current errors themselves [12].

The tidal energy extraction is expected to mainly affect cetacean and benthic communities. The primary environmental impact is the habitat modification. This change can generate problem in the reproduction and recruitment areas of these communities [13]. The installation of tidal arrays can also affect seasonal patterns of vertical mixing and water stratification [14], decrease currents and tidal amplitude [13] or bring increase water clarity through reduce sediment transport [15].

Several technological challenges lie ahead for the commercial use of tidal marine energy. In 2009, Cruz et al. [7] considered  $V_{msp}$  values  $> 3$  m/s as excellent,  $> 2$  m/s as good, and  $> 1.8$  m/s as worthy of investigation, given the available technology at the time. This range has been lowered to 1 m/s [16] with recent technological developments. In studies of marine renewable energies, 2D (vertically averaged) and 3D models have been used to describe areas where measurements are scarce. These models are usually validated with elevation of sea level, due to the availability of tide gauges records for several years. The recent availability of ADCP data has allowed for a better validation against observed currents. Of all areas in southern Chile, the Chacao Channel has been a place of interest for tidal energy, since tidal currents can exceed 4 m/s. This location has been previously studied using observations and models [6,17–19]. Other studies of tidal energetic channels have found a marked tidal asymmetry of the ebb/flood regime and in their spatial variability [9]. Recent studies advise against the use of depth-averaged 2-D studies of tidal energy [20,21], because the velocity profile is better represented in the 3-D case, particularly in the vicinity of tidal arrays. The 2D depth-averaged numerical models are computationally more efficient and useful for a first approximation of the resource but for accurate assessments 3D models are required. The uncertainties associated with resource assessments are greater in deep water [21]. Wave-current interaction is also a factor to consider [22,23], since it can impact up to 20% of tidal power under extreme wave conditions.

## 2. Study area

The Chilean Inland Sea (CIS) considered in this study includes the seas from the northern part of the Chilean Patagonia, between  $41.5^\circ$  S and  $46.5^\circ$  S. It comprises several microbasins, fjords and channels (Fig. 1). The main sub-basins are the Reloncavi Sound, the Gulf of Ancud, the Gulf of Corcovado, the Guafo Mouth and the Moraleda Channel (including the Elephant Estuary). In the north, the CIS connects with ocean waters through the Chacao Channel ( $41.83^\circ$  S,  $73.53^\circ$  W), while in the southern part a large number of shallow channels (around the Chonos Archipelago) connect the ocean with the Moraleda Channel. The Chacao Channel is approximately 40 km long and 4 km wide, and contains one of the most extensive fjords and channels systems in the world [24]. The bathymetry is markedly different to the north and south of the Guafo Mouth. The northern portion is composed of the Gulfs of Corcovado and Ancud, with a width of 50 km, and Reloncavi Sound at the far north, with a width of 30 km. The southern part is composed of a series of channels, the main one being the Moraleda Channel (20 km), and a major input of freshwater from Aysen Sound. During the last decades, salmonid farming and mussel aquaculture have increased dramatically in the CIS, with concomitant urban and industrial development. Most regional studies have focused on evaluating changes in the environmental conditions associated

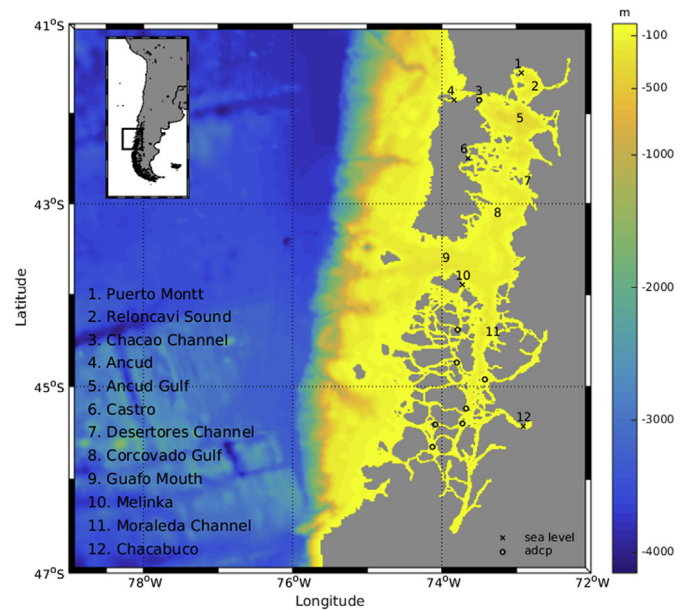


Fig. 1. Bathymetry of the Chilean Inland Sea used in the oceanic model. The study area is between  $41$  and  $47^\circ$  S and  $72$ – $79^\circ$  W. The circles and crosses correspond to ADCP and tide-gauge measurements, respectively.

with aquaculture [25–29] and/or trying to better understand the tides behavior, coastal circulation and estuarine dynamic of this area [30–34].

General circulation in the CIS can be classified as a two-layer estuarine system, with water exchange between the interior sea and the Pacific Ocean [35]. This system consists of a top layer of roughly 100 m of stratified freshwater and a more saline, stable, quasi-homogeneous interior or deep layer from 100 m depth to the bottom [36]. Some studies mention a third layer with a compensatory effect of surface winds blowing to interior fjords [30,37] and/or non-linear tidal effects produced at the estuary head [31,38]. Two zones have a combination obstruction-constriction control circulation: the Desertores Channel ( $42.7^\circ$  S,  $72.83^\circ$  W) and the Meninea Constriction in the Moraleda Channel ( $45.25^\circ$  S,  $73.75^\circ$  W). These topographic characteristics control the exchange of different water masses, permitting ventilation in the micro-basins [39]. The interaction with these constrictions can produce internal waves and jets that influence the tidal currents [40].

Tides and winds are the main forces generating the currents in the interior and the exterior of the CIS [41]. The tidal regime throughout the CIS is mostly influenced by semi-diurnal tidal currents [17]. Tidal waves enter via the Guafo Mouth, moving northward through the Gulf of Corcovado or south through the Moraleda Channel [6,18]. Aiken [6] implemented a 2D numerical model of the study area, with a 1.5 km resolution in the inland sea. Several numerical experiments were done for eight tidal constituents ( $M_2$ ,  $N_2$ ,  $S_2$ ,  $K_2$ ,  $K_1$ ,  $O_1$ ,  $P_1$ , and  $Q_1$ ) with a model run for each constituent. Each run lasted six days, hourly results from the last two days were compared to available data. Bottom friction was parameterized with a quadratic term, and a different drag coefficient for each simulation was used. The high tides observed in the area near the city of Puerto Montt ( $41.5^\circ$  S,  $72.93^\circ$  W) could be explained by a resonance effect of the wave as it travels through the Gulf of Ancud that is added to the tidal wave entering through the Chacao Channel. During spring tides, there are large sea level variations in the northern CIS, which can be associated with high tidal currents, particularly in narrow steps and shallow channels connecting different micro-basins. In contrast, during neap tides, sea level

variations are relatively small, and tidal currents are drastically reduced. Tidal modelling is highly sensitive to the resolution of the complex coastal geometry, due to resonance, especially in the CIS [6]. Furthermore, topographic features as sills or constrictions can be produce non-line  $M_4$  or processes of bottom friction and advection that result in tidal constituents of high frequency as quarter-diurnal tides (e.g., overtide) and sixth-diurnal tides (e.g., overtide  $M_6$ ) [17].

### 3. Methodology

#### 3.1. Numerical model

Our study is based on high-resolution numerical simulations of the CIS using the CROCO (Coastal and Regional Ocean Community) numerical model. This model is an updated version of the ROMS-AGRIF model [42], that includes a non-hydrostatic kernel capable of resolving very fine scales and reproducing the interaction between different spatial scales using nesting. This is a 3D numerical model of free-surface oceanic circulation that solves the equations in an Earth-centered rotating environment. In our case, we use depth-averaged (barotropic equations), which are solved using a single homogeneous layer. The model solves the barotropic mode separately using a time step of 1 s [43]. Terrain-following coordinates are used on an Arakawa-C structured grid [44] using a discretization of finite volumes. We use a  $k - \omega$  model from the Generalized Length Scheme [45] for turbulence closure in the parametrization of vertical mixing and a Smagorinsky model for lateral mixing.

The model domain extends along a meridian from  $41^\circ$  S to  $47^\circ$  S and zonally from  $79^\circ$  W to  $72^\circ$  W, with a spatial resolution of  $1/72^\circ$  (Fig. 1). The model bathymetry is a blended product based on the GEBCO08 dataset [46] for the open ocean and on many different soundings provided by the Chilean Naval Hydrographic and Oceanographic Service (SHOA) in the coastal zone. In order to reduce pressure gradient error and make more stable numerical simulations, bathymetric smoothing was required in all sigma coordinate models [47]. A Hanning filter was used to ensure that there was no 2DX noise in the topography. The minimum water depth was set at 10 m, and the coastline was manually edited to improve the representation of small fjords and channels, based on the topography and nautical information provided by SHOA.

Hydrographic information for the boundary and the initial conditions were taken from World Ocean Atlas 2009 [48,49]. Tides in our model simulation were forced using sea surface elevation and the barotropic velocity from the TOPEX/Poseidon global tidal inverse solution (TPX08) [50]. This product improves tidal predictions for coastal areas compared to older versions. The initial tide was adjusted to January 5, 2016, coinciding with a spring tide. Ten tidal constituents were used simultaneously. Four semi-diurnal constituents ( $M_2$ ,  $S_2$ ,  $N_2$ ,  $K_2$ ), four diurnal constituents ( $K_1$ ,  $O_1$ ,  $P_1$ ,

$Q_1$ ) and the long-period lunar fortnightly ( $M_f$ ) and monthly ( $M_m$ ) tides. The simulation period extended for 1 month (January 2016), and the model outputs were recorded hourly, but the first 3 days are not used in our analysis. Finally, in the open boundary conditions, a Flather scheme for the barotropic velocities was used. A constant value of  $1.65 \times 10^{-3}$  m/s was used for bottom drag.

#### 3.2. Model validation

To evaluate the model simulation, we used sea level data from five coastal tide-gauge stations in the CIS: Puerto Montt, Melinka, Chacabuco, Castro, and Ancud (Fig. 1). This tide gauges are monitored by SHOA, official, technical and permanent service of State (<http://www.shoa.cl/php/nivel-del-mar>). The original data of 1 or 2 min were edited to remove spikes and outliers. Hourly averages were then computed for the study period (January 2016). Further, data from eight ADCPs (Teledyne RD Instruments of 300 kHz and 150 kHz nominal frequencies) were also used in model evaluation. The ADCP locations are represented by circles in Fig. 1. The ADCP data were measured by the Chilean Fisheries Development Institute (IFOP) between 2010 and 2015. Note that all current records used here are longer than 1 month, but the data were obtained in different years and months. Currents were recorded every 10 min using different vertical resolutions, depending on the mooring depth (Table 1). Pressure sensors from the ADCPs were also used as an estimator of sea level elevation used for model validation.

The ADCP data were processed following the procedure given by Valle-Levinson and Atkinson [51]. Velocity errors greater than 5 cm/s and good percentage of data less than 85% were discarded. Depths were calculated with the pressure sensor, referencing the surface bins. Values from pitch, roll, and heading larger than those suggested by the manufacturer were also discarded. Small gaps (smaller than 3 h) were filled using linear interpolation. We estimated the barotropic current from the ADCP data by averaging in depth the velocity components at each time-point. The ADCP data were obtained with the instrument mounted on a moored platform, and data covered most of the water column ensuring a better approximation of the barotropic component [52]. These averaged currents were then used to compare against the modeled currents.

The root mean square error (RMSE), normalized root mean square error (NRMSE), Pearson correlation coefficient ( $r$ ), and bias and normalized bias were used to validate the model. Modeled sea level (MSL) time series were compared with tide gauge data at five locations (Table 2, see also Fig. 1, crosses labeled from 1 to 5). The MSLs showed good correlation with the observed time series ( $r > 0.9$ ) although it overestimated the tidal range in all stations (NRMSE  $< 10\%$ ). The Puerto Montt time series presented the best correlation ( $r = 0.96$ ), while Ancud (location 1 in Fig. 1) showed the lowest correlation, although it was still relatively high ( $r = 0.91$ ). The sea level ranges in the stations inside CIS increased from 3 m in the south to 8 m in the north during spring tides. In general, sea

**Table 1**  
Location of the ADCP stations, time period, and bins information.

Name	Latitude	Longitude	Date start	Date end	Frequency (kHz)	Height of first bin (m)	Bin depths (m)
Darwin	-45.4060	-74.0819	2015/04/01	2015/05/22	307	6.19	4
Darwin Erraz	-45.3967	-73.7192	2011/10/06	2011/11/06	154	6.35	2
Pta Garrao	-44.3873	-73.7882	2014/08/31	2014/11/16	307	4.21	2
Gaviota	-45.2407	-73.6753	2015/06/12	2015/08/01	307	4.21	2
Meninea	-45.2407	-73.6753	2015/06/11	2015/07/11	307	4.22	2
Perez Sur	-44.7430	-73.7950	2014/05/28	2014/07/02	307	4.21	2
Pulelo	-41.8533	-73.4921	2014/04/22	2014/05/14	307	3.21	1
Vicuna	-45.1274	-74.1274	2015/03/02	2015/05/20	307	6.18	4

**Table 2**  
Statistical comparison between coastal tide-gauge measurements and numerical simulations.

Station	r	RMSE (cm)	NRMSE (%)	BIAS (cm)	NBIAS (%)
Ancud	0.9	23	10	-2.4	-1
Puerto Montt	0.95	51	8	-2	-0.3
Castro	0.94	40	7	-2.6	-0.5
Melinka	0.93	20	8	-2	-0.8
Chacabuco	0.93	27	10	-0.1	0.02

level is about two times larger during spring versus neap tides, and the model could reproduce this variability. Puerto Montt shows the highest tidal ranges (Fig. 2b), with maximum values of 7.5 m during spring tides and 3.9 m during neap tides. Conversely, Ancud has the smallest tidal ranges (Fig. 2a) of 0.96 and 1.75 m during neap and spring tides, respectively. Castro (Fig. 2c) presented a elevation of 3.2 m and 6.1 m during neap and spring tides, respectively. Melinka had a elevation of 1.4 m during neap tides and 2.7 m during spring tides (Fig. 2d). Finally, Chacabuco had very similar elevations in comparison with Melinka (Fig. 2e) with neap and spring tides of 1.9 m and 3.6 m. As with the elevation, the phases of the sea level time series are also well replicated by the model, as were the modulations observed during spring and neap tides.

We used ADCP data from eight locations (Table 1) to evaluate modeled tidal currents. Tidal current ellipses were calculated for the two dominant semi-diurnal tidal constituents ( $M_2$  and  $S_2$ ). A comparison of the major semi-axes are presented in Fig. 3, as well as the amplitude of  $M_2$  and  $S_2$  estimated for the sea level. In this comparison, we also used sea level time series derived from the ADCP pressure sensors. These measurements complement the five tide-gauges in the study region by adding eight extra locations. The RMSE for the adjusted amplitude to all sea level records was 18 cm for  $M_2$  (Fig. 3a) and 6 cm for  $S_2$  (Fig. 3b), while the scatter index (SI, RMSE normalized) was less than 15%. RMSE for the phase was less than 15° (not shown), which was estimated by using only the tide-

gauge data, since ADCP data included different periods than the model simulation (Table 1). The main axes of depth-averaged tidal currents showed RMSEs of 5 cm/s (Fig. 3a) and 3 cm/s (Fig. 3b) for  $M_2$  and  $S_2$ , respectively, and the scatter index was less than 12%.

In summary, the model reproduced the sea level elevation variability, the amplitudes and phases of the dominant tidal constituents reasonably well in the Chilean Inland Sea, including the large modulation observed between spring and neap tides (Table 2 and Fig. 3). The main mechanisms that generate the tidal resonance, and the resulting large amplitude of the semi-diurnal harmonics in the northern side of the CIS, seem to be reconstructed well by the model. Tidal currents were also reasonably well simulated by the model, considering the complex coastline and topography, and their simplifications in the model. A better representation of the tidal currents in a specific location would require local models with much higher resolution and more realistic bottom topography and coastlines.

### 3.3. Tidal variability

We used  $T_{TIDE}$  [53], a Matlab toolbox, to calculate and separate the main tidal constituents from modeled and observed time series. This consisted of calculating the harmonic amplitudes and phases of a given set of tidal frequencies. Here, harmonic analysis assumes that the sea level and current fluctuations can be expressed by the sum of several harmonic functions of known frequencies. According to the characteristics of the tidal pattern, the tides can be classified with the form factor,  $F$ . This dimensionless number is a ratio between the main diurnal and semi-diurnal amplitudes of the constituents, defined as:

$$F = \frac{K_1 + O_1}{M_2 + S_2} \tag{1}$$

where  $K_1$ ,  $O_1$ ,  $M_2$ , and  $S_2$  are the respective tidal amplitudes of the harmonic constituents. Hence, tides are classified as one of four

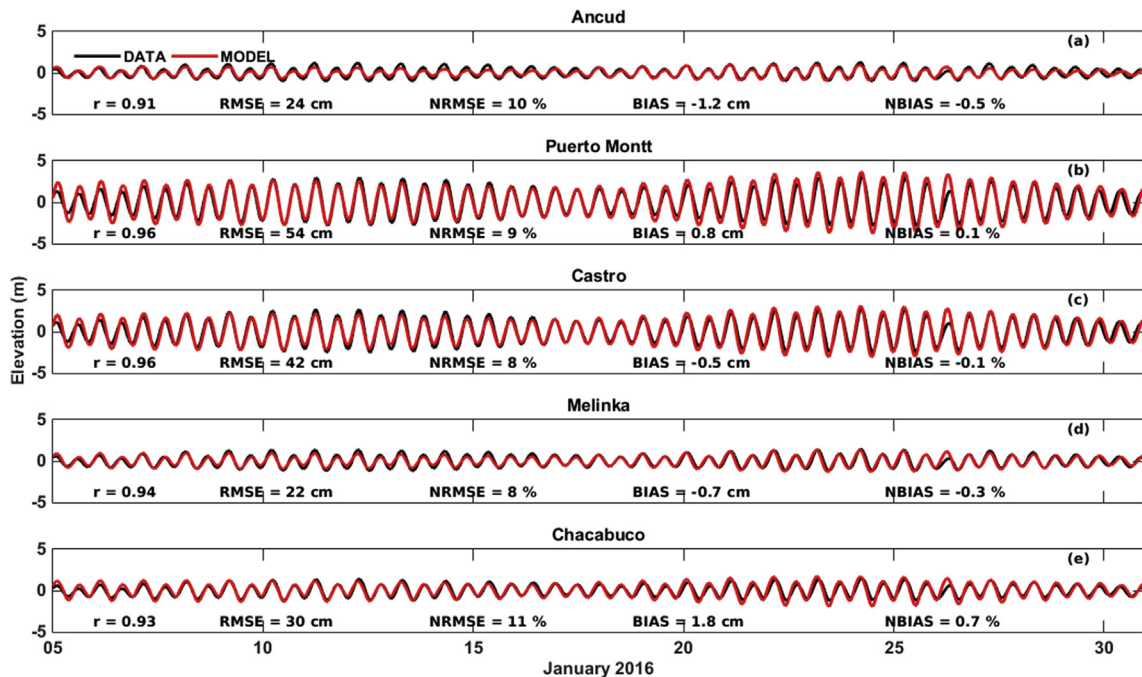


**Fig. 2.** Sea level comparison between tide-gauge measurements (black lines) and oceanic model outputs (red lines). (For interpretation of the references to colour in this figure legend, the reader is referred to the Web version of this article.)

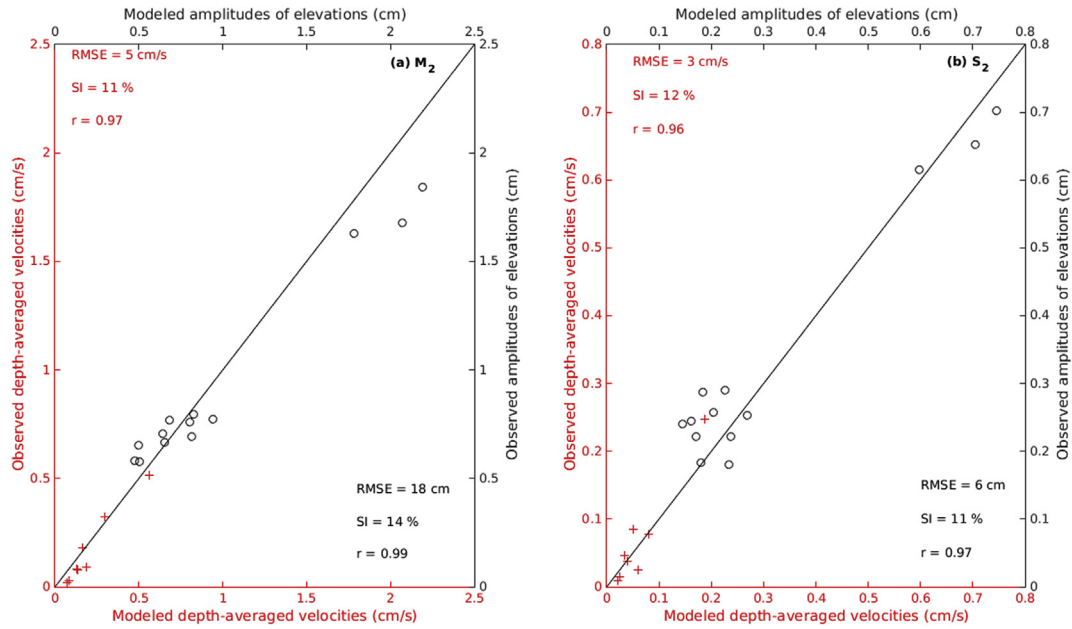


**Fig. 3.** Model-data comparisons and statistics. The black circles are amplitudes of elevations and the red plus sign are depth-averaged velocities of (a)  $M_2$  and (b)  $S_2$ . (For interpretation of the references to colour in this figure legend, the reader is referred to the Web version of this article.)

types, semi-diurnal ( $F < 0.25$ ), diurnal ( $F > 3$ ), mixed mainly semi-diurnal ( $0.25 < F < 1.5$ ), or mixed mainly diurnal ( $1.5 < F < 3$ ). The tidal current form ratio ( $F_u$ ) is defined using the depth-averaged tidal current amplitude instead of tidal elevation amplitude.

$$F_u = \frac{K_{1u} + O_{1u}}{M_{2u} + S_{2u}} \quad (2)$$

The lunar variability (spring-neap tides) in the tidal currents can be quantified using the ratio,  $R$  [54]:

$$R = 1 - \frac{S_2}{M_2} \quad (3)$$

where  $M_2$  and  $S_2$  are the depth-averaged tidal velocity amplitudes for the semi-diurnal lunar and semi-diurnal solar frequency, respectively. Large values of  $R$  ( $M_2$  larger than  $S_2$ ) are desirable for energy exploitation, because tidal ranges experience only minor changes week to week. In contrast, when both  $M_2$  and  $S_2$  are of similar magnitude, tidal ranges experience large differences between neap (both constituents are about  $180^\circ$  out of phase) and spring (both constituents are about in phase) tides.

The potential/theoretical output power of a marine current turbine is related to the kinetic energy of the fluid [55]. The instantaneous maximum power per unit area of flow (tidal-stream power density),  $P_{MAX}$  [11], is given by:

$$P_{MAX} = \frac{1}{2}MU^2 = \frac{1}{2}\rho U^3 \quad (4)$$

where  $M$  is the mass of the seawater,  $\rho$  is the density of seawater, and  $U$  is the depth-averaged velocity. Due to potential losses in power extraction, this equation must be modified, with limitations related to turbine efficiency, which can be incorporated to (4) by using a power coefficient ( $C_p$ ). Currently, there are turbines with more than 48% theoretical efficiency, but our calculations use a conservative value of  $C_p = 0.4$ . Therefore, the tidal-stream power per square meter for a turbine is

$$P = \frac{1}{2}C_p\rho U^3 \quad (5)$$

To quantify the output power, we compare the values of barotropic currents modeled with the power curve of SeaGen – S 2 MW turbine ([www.atlantisresourcesltd.com/services/turbines](http://www.atlantisresourcesltd.com/services/turbines)). The SeaGen system is an up to 1.0 MW horizontal axis turbine complete with an active pitch. The rotor blades have a diameter of the 20 m and a swept area of  $648 \text{ m}^2$  for 2 rotors. This turbine has a *cut-in* tidal speed of 1 m/s and a rated power at 2.5 m/s. For higher tidal speeds the output power is regulated at rated power. Finally, the effective power output is defined as the turbine power curve times the number of hours for a given velocity.

## 4. Results

### 4.1. Characteristics of the modeled tides

The oceanic tide propagates southward along the Chilean coast and forces coastal tidal waves into the CIS, mainly through the Guafo Mouth, propagating northward along the Gulf of Corcovado and southward along the Moraleda Channel. This propagation is represented by the phase relative to Greenwich meridian. A standing wave with constant phase but increasing amplitude can be observed from the Guafo Mouth to the Gulf of Ancud, with a small phase change toward Reloncavi Sound and from Melinka to San Rafael Lagoon. There is a clear amplitude amplification in each semi-diurnal tidal constituent from the Guafo Mouth to the north and south. The  $M_2$  amplitude constituent is 28% greater in Puerto Montt (2.5 m) in comparison with the amplitude observed in the open ocean (0.7 m). As observed in the tide-gauges in the model validation section, the tidal amplitude of  $M_2$  is three times larger than that of  $S_2$  at northern part of the CIS. The dominant diurnal constituents,  $K_1$  and  $O_1$ , also show amplification toward the northern CIS. The amplitude of the  $K_1$  harmonic constituent also is 28% greater in Puerto Montt (0.32 m) in comparison with the Guafo Mouth (0.23 m). Unlike the semi-diurnal case, the amplification occurs symmetrically in the northern and southern CIS. The tidal

amplitude of  $K_1$  is two times larger than  $O_1$ , and  $Q_1$  is one order-of-magnitude smaller. The  $O_1$  and  $Q_1$  amplitudes are less than the RMSE values obtained for the elevation of sea level (Fig. 2).

The phase remains homogeneous in the Guafo Mouth, and enters to the interior of the CIS, behaving like a mix of standing and progressive waves to the north and south. The major and minor axes of the tidal current ellipse for  $M_2$  and  $K_1$  constituents summarize the main characteristics of this propagation pattern (Fig. 4). The patterns are similar in shape with one order-of-magnitude difference in amplitude. The tidal current ellipses for other harmonic constituents not show here, because have the same circulation pattern but with smaller amplitudes.

Diurnal and lunar variabilities were calculated as the ratio  $F_{li}$  (Eq. (2)) and the spring-neap ratio  $R$  (Eq. (3)) in the CIS (Fig. 5). The CIS is modulated mainly by semi-diurnal tides in the north and mixed mainly semi-diurnal in the south and open ocean. Note that the tidal type at the Deserotores Channel is semi-diurnal, and at the Chacao Channel, it is mixed mainly semi-diurnal (Fig. 5a). Likewise, the northern CIS has a greater tidal variability between spring-neap flows ( $R \sim 0.62$ ) in comparison with the southern CIS ( $R \sim 0.75$ ). The Deserotores Channel presented greater differences between spring and neap tides than the Chacao Channel (Fig. 5b).

#### 4.2. Assessment of tidal current energy resources

A preliminary site selection study is the first step to identify potential locations for exploring the use of marine renewable energy. Only the tidal energy resource was considered, discarding other criteria, such as distance to the electricity grid, topography, fishing concessions, or onshore protected areas. Current turbine technology allows for operating in current speeds greater than 1 m/

s. We use a cut-in speed of 2 m/s for a more conservative study. The modeled barotropic tidal currents show two potential zones for this type of energy: the Chacao Channel and the Deserotores Channel. The magnitude of the currents in the narrowest zone in the Chacao Channel overcome the 2 m/s cut-in speed more than 70% of the month. In the nearby areas, this frequency varies between 20% and 50%. In contrast, the Deserotores Channel shows velocities that overcome 2 m/s during 20%–30% of the month. Both cycles of spring tides are associated with velocities greater than 2 m/s 50% of the month. Likewise, a 25% value can be associated with just flood tides during spring tides.

To visualize this variability in the tidal-stream, we used the maximum current value of a complete diurnal tidal cycle of spring and neap tides. The barotropic currents in much of the northern CIS have values less than 0.5 m/s, with faster currents in the channels and constrictions. For much of the neap and spring tides, zones of the Chacao and Deserotores Channels are shown to be the areas with the highest velocities. During neap tides, these velocities are in the order of 3.5 m/s in the Chacao Channel and 2 m/s in the Deserotores Channel (Fig. 6a). These velocities can almost double during spring tides, with values close to 6 m/s and 4 m/s in the Chacao and Deserotores Channels, respectively (Fig. 6b). There is a zone to the west of the Deserotores Channel with velocities greater than 2.5 m/s in spring tides, but areas like this are not considered in the energy assessment because their velocities are less than 10% of the month.

The amount of available tidal energy depends significantly on the tidal-stream intensity. For a single turbine, a good indicator to evaluate tidal-current energy is the potential mean power density [11]. The spatial patterns of currents and potential power density are similar in each tidal phase. If neap tides are considered, the Chacao Channel becomes more bounded, with values of  $10 \text{ kW/m}^2$ ,

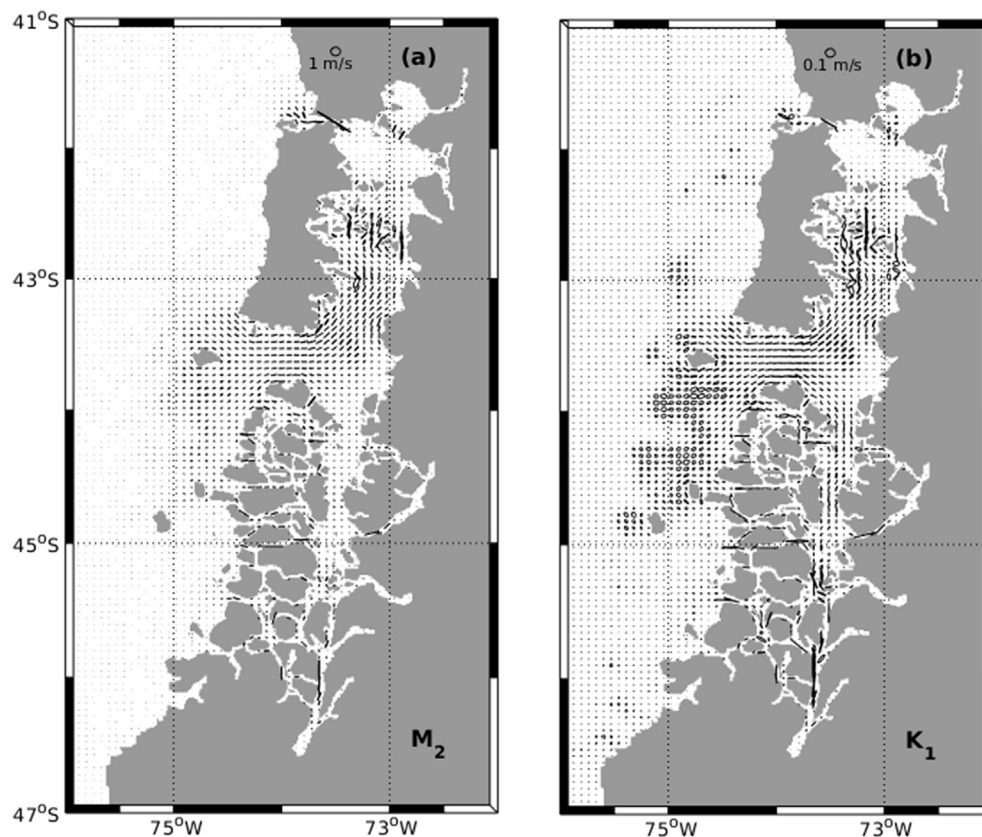
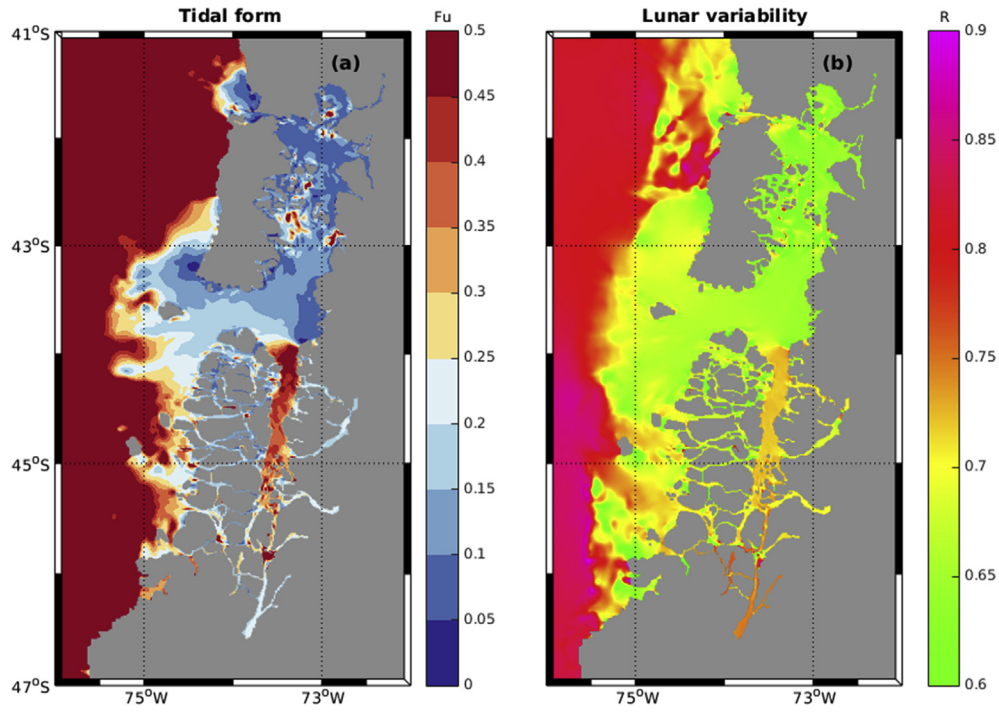
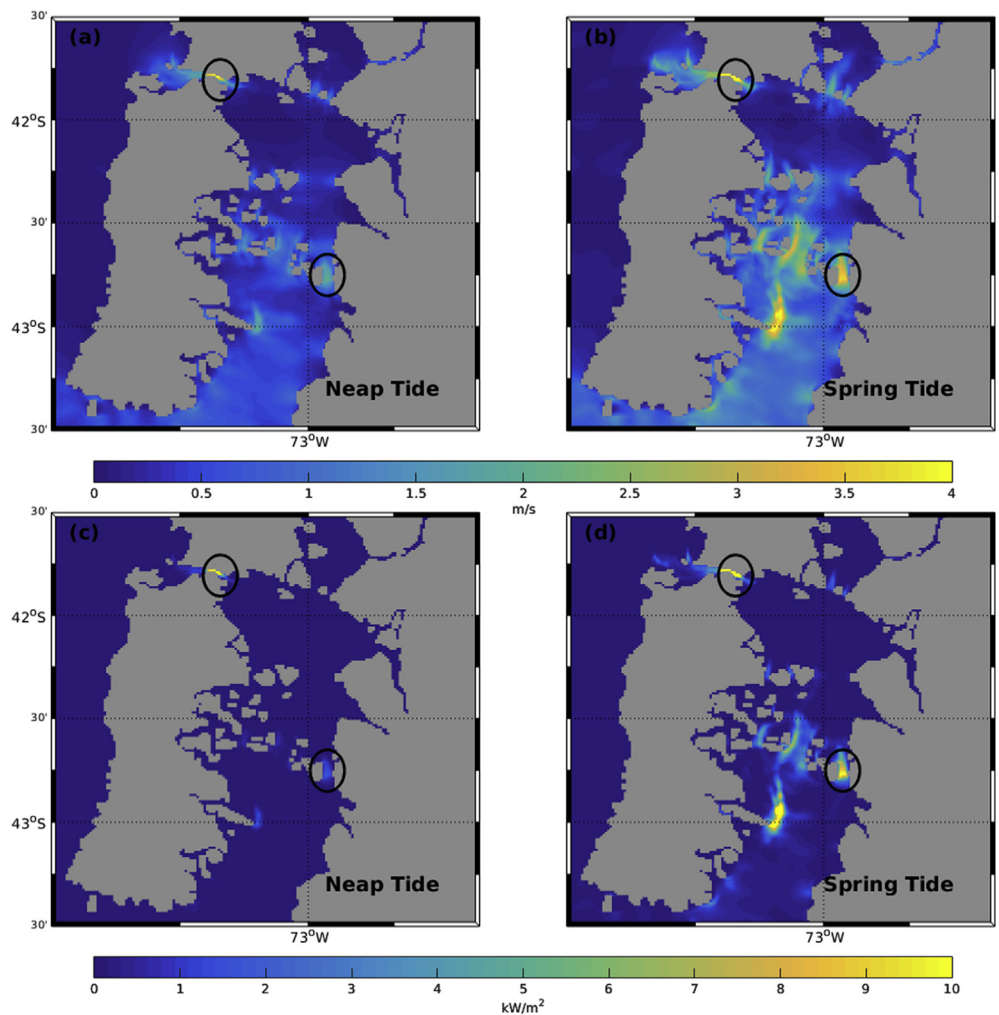


Fig. 4. Major and minor axes of the tidal ellipses. Ellipse axes are shown every five grid points in latitude and longitude direction. (a)  $M_2$  with 1 m/s scale. (b)  $K_1$  with 0.1 m/s scale.



**Fig. 5.** (a) Spatial variability in the tidal current form ratio,  $F_u$  (Eq. (3)).  $F_u$  has been capped at an upper bound of 0.5 in order to distinguish between semi-diurnal and mixed mainly semi-diurnal tides. (b) Spatial variability in the simulated spring-neap cycle of tidal currents,  $R$  (Eq. (4)). Values of  $R < 0.6$  have been set to 0.6 for better visualization of potential TEC sites.



**Fig. 6.** Maximum depth-averaged velocities in a diurnal tidal cycle in (a) neap tide, and (b) spring tide. Simulated power density of distribution at the (c) neap tide, and (d) spring tide. In (d) note that the values in Chacao Channel are of the order 40 kW/m<sup>2</sup>.

and the Desertoires Channel is less energetic, in the of the order 2  $kW/m^2$  (Fig. 6c). During spring tides, the available resources are higher, with the Chacao Channel reaching a peak of 40  $kW/m^2$ , while the Desertoires Channel generates 10  $kW/m^2$  (Fig. 6d).

The evolution over time of tidal-stream power density at a point inside both channels confirms these values and shows their variability during the month. The energy resource is significantly higher during spring tides compared to neap tides at both locations. The diurnal variability of flood and ebb tides in the Chacao Channel can be almost four times as large during spring tides when compared to neap tides, with the mean power density close to 5  $kW/m^2$  in the Chacao Channel, and with maximums of 40  $kW/m^2$  and 10  $kW/m^2$  during spring and neap tides, respectively (Fig. 7a). In comparison, power density is significantly lower in the Desertoires Channel, with maximum power densities of 8  $kW/m^2$  and 1.5  $kW/m^2$  during spring and neap tides, respectively, with a mean value of 0.9  $kW/m^2$  (Fig. 7b).

These values for power density are a power extraction theoretical efficiency of 60%. A better option for tidal assessment use the rated efficiency of a real turbine. In this case, we used the power curve for the SeaGen-S 2 MW turbine, which operates at velocities between 1 and 4 m/s. We counted the number of hours in which the velocities are in a certain range (separated each 0.5 m/s), and calculated the power output in MWh. The velocities less than 1 m/s in the Chacao Channel occur over 133 h (5.5 days) during one month, and there are 519 h (21.6 days) where the turbine can be operative (Fig. 8a). Note that there are 69 h (almost 3 days) where the turbine cannot operate because it is subjected to velocities > 4 m/s. This means that this turbine could ideally produce 739 MWh in one month at this location (Fig. 8b). In contrast, the velocities in the Desertoires Channel apparently follow a Gaussian distribution, centered in the range of 0.5–1 m/s. The turbine can be operative 424 h (17.6 days), but it would experience only 48 h of rated power (Fig. 8c). Despite this, the turbine could deliver 348 MWh in a

month from the Desertoires Channel (Fig. 8d), approximately half that produced in the Chacao Channel.

## 5. Discussion

The present study was designed to determine the effect of lunar variability on tidal-stream assessment in areas where  $M_2$  and  $S_2$  oscillate almost in phase resulting in an amplification of the sea level elevation during spring tides and a decrease of sea level elevation during neap tides. Prior studies have noted the importance of considering tidal lunar phase variability in annual practical power generation [14]. In Chile, tidal energy assessments have been conducted through technical reports. These assessments consider the maximum values of tidal currents and do not take into account the variability of the different tidal phases. These studies have been carried out with both *in situ* measurements and numerical models.

An acceptable barotropic numerical simulation of the Chilean Inland Sea (CIS) must be capable of reproducing the relatively larger amplitudes of the tidal range in the northern section (over 7 m at Puerto Montt and Reloncavi Sound) in contrast with the tidal range at the Guafo Mouth (2 m). In other words, the model must be able to reproduce the resonance effect that occurs in the tidal range when entering the CIS [6]. Tidal propagation and amplification in the interior of the CIS are consistent with other simulations of barotropic models in Chilean Patagonia [6,18]. The RMSE values between tide-gauges and elevation of numerical model shown an overestimation between a 8% and 11% in the points analyzed. These error ranges could be decreased by improving bathymetric and coastline resolutions and by changing spatially the value of the bottom drag coefficient [18]. Note that the CROCO model does not allow this spatial variability. The 2D numerical model implemented by Aiken [6] only used one tidal constituent in each simulation. This methodology does not allow for interactions between different tidal harmonics affecting the generation of nonlinear tidal effects, such as overtides ( $M_4$ ,  $M_6$ ). These overtides have been registered in

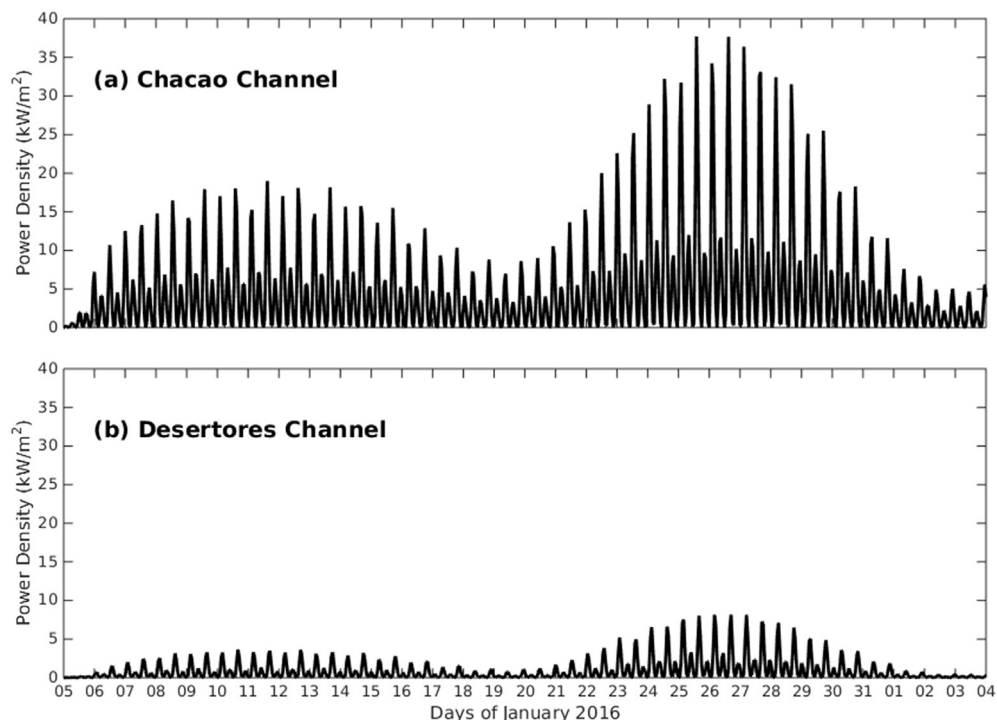
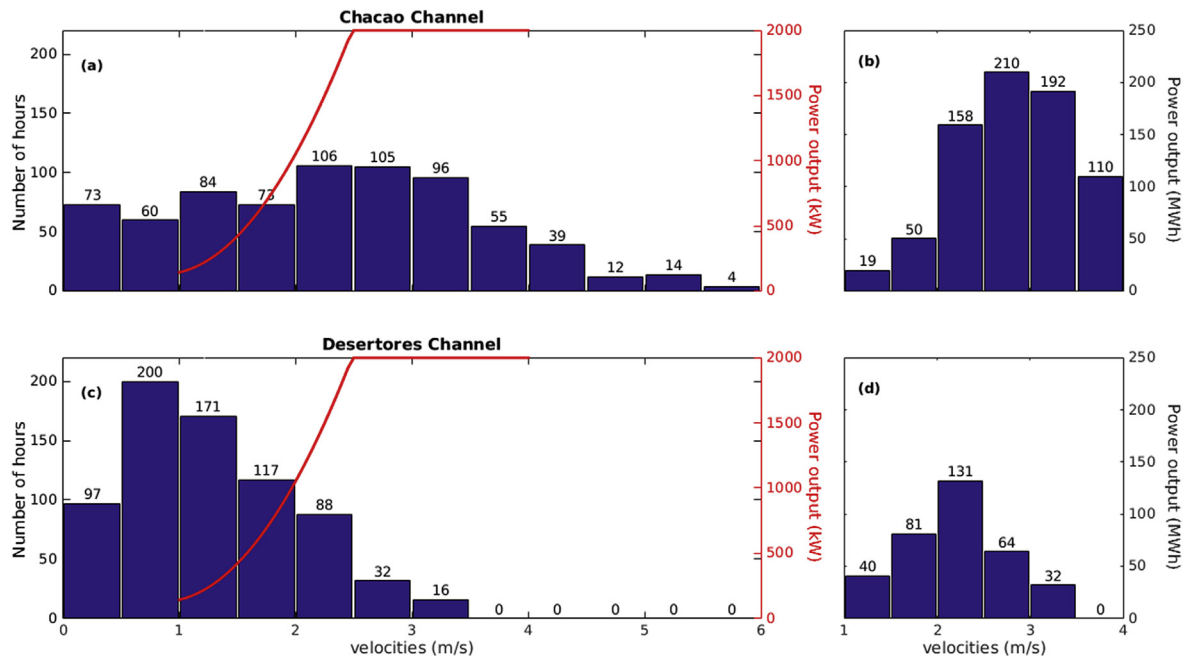


Fig. 7. Simulated power density at the (a) Chacao and (b) Desertoires Channels.



**Fig. 8.** (a) Theoretical Power curve of a SeaGen-S 2 MW turbine in kW (black line) and histogram of velocities at the (a) Chacao Channel, and (c) Desertoires Channel. (b) Effective power output in MWh at the (b) Chacao Channel, and (d) Desertoires Channel.

the Chacao Channel [30] and appear in the tide-gauges as in the numerical simulations, demonstrating the importance of allowing them to interact. Our simulation used ten tidal constituents simultaneously with a constant value of bottom drag. The model reproduced the overtides, but these were not analyzed in this work.

The amplitude validation of the main semi-diurnal and diurnal constituents are comparable to other tidal energy modelling studies in other regions, such as the NW European shelf [8,9]. An important point to consider is that the density of oceanographic information is limited in the CIS [41], and usually focuses on coasts and middles of small channels (Fig. 1). Error ranges could be diminished if data inside the larger areas of the CIS, such as the Gulfs of Ancud and Corcovado, were available. Although our model shows a 3–5 cm/s RMSE in tidal currents and 6–18 cm RMSE in the amplitudes of the  $M_2$  and  $S_2$  harmonics (Fig. 3), the results about tidal-stream energy assessment during spring and neap tides are still valid.

There is a different level of spring/neap asymmetry between tides in the Chacao and Desertoires Channels. The values of  $F_u$  as  $R$  explain the main differences found between sites, specifically the low value of  $R$  in the Desertoires Channel. Higher values of  $F_u$  generally generate less practical power, and larger values of  $R$  will generate a more continuous energy yield, because the variability between spring and neap tides is relatively low [9] indicating power density is less continuous in the Desertoires Channel.

Cruz et al. [7] identified some potential sites for tidal energy extraction, including the Chacao Channel and regions of the Gulf of Corcovado (the Desertoires Channel in our case). Guerra et al. [19] estimated an average of  $5 \text{ kW/m}^2$  in kinetic power density in the Chacao Channel using a 3D model. This value is corroborated in this study with our 2D model. We complement this value by separating the assessments during spring and neap tides, finding maximum values of  $40 \text{ kW/m}^2$  and  $10 \text{ kW/m}^2$ , respectively. The Desertoires Channel showed a power density of  $0.9 \text{ kW/m}^2$  on average, but with greater values during spring tides.

Although the currents are clearly faster in the Chacao Channel

than the Desertoires Channel, due to the range of operations permitted by turbines, both are potential sites given the potential and theoretical output power obtained from the model. Both sites may be good options for testing and developing tidal energy. Other considerations, such as navigation routes, fishing zones, aquaculture, and tourism, could be incorporated. Further research should be undertaken to investigate tidal residual circulation. The current velocity values could be significantly modified by the effect of wave field [56]. Hashemi [57] said that the effect of wave can reduce the tidal power by 15% and up to 20%, for mean winter or extreme wave conditions, respectively. A further study with more focus on the wave current interactions is therefore suggested.

## 6. Conclusions

The aim of the present research was to evaluate possible sites for tidal-stream extraction in Chilean Patagonia and determine the importance of the lunar phase in its assessment. This study has shown that when the amplitude differences between spring and neap tides are significant, one should consider the entire tidal cycle and not simply average or maximum values. We find two potential zones, each with values of tidal-stream velocities greater than 1 m/s: the Chacao Channel and the Desertoires Channel. Tidal energy yield is more continuous in the Chacao Channel in comparison with the Desertoires Channel, where tidal-stream extraction is possible only during spring tides. During spring tides, the power density maximum is  $40 \text{ kW/m}^2$  in the Chacao Channel and  $10 \text{ kW/m}^2$  in the Desertoires Channel, and a SeaGen-S 2 MW turbine could obtain a maximum power output of 739 MWh and 348 MWh.

The findings of this investigation complement those of earlier studies in the Chilean Inland Sea. This investigation shows that it is possible to assess tidal-streams using a barotropic model. In turn, it allows further research into potential sources of non-conventional renewable energy. Further research might explore other processes, including nonlinear effects produced by resonance, the contribution of the advection product of river flows, or the contribution of wind variability. Also, it would be interesting to calculate how

much tidal-stream energy could be harnessed by small rural populations and aquaculture farms.

## Acknowledgments

Oswaldo Artal was funded by a national CONICYT grant (CONICYT doctorate scholarship 21140379). Powered@NLHPC: This research was partially supported by the supercomputing infrastructure of the NLHPC (ECM-02). We thank the staff of IFOP-Castro for providing the ADCP data. Comments by two anonymous reviewers were very helpful to improve our manuscript.

## References

- [1] D.G. Mediavilla, H.H. Seplveda, Nearshore assessment of wave energy resources in central Chile (2009–2010), *Renew. Energy* 90 (2016) 136–144, <https://doi.org/10.1016/j.renene.2015.12.066>.
- [2] S. Nasirov, C.A. Agostini, C. Silva, An assessment of the implementation of renewable energy sources in the light of concerns over Chilean policy objectives, *Energy Sour. Part B Econ. Policy*. 12 (2017) 715–721, <https://doi.org/10.1080/15567249.2017.1292330>.
- [3] C. Mattar, M.C. Guzmán-Ibarra, A techno-economic assessment of offshore wind energy in Chile, *Energy* 133 (2017) 191–205, <https://doi.org/10.1016/j.energy.2017.05.099>.
- [4] S. Kelly-Richards, N. Silber-Coats, A. Crootof, D. Tecklin, C. Bauer, Governing the transition to renewable energy: a review of impacts and policy issues in the small hydropower boom, *Energy Policy* 101 (2017) 251–264, <https://doi.org/10.1016/j.enpol.2016.11.035>.
- [5] J.W. Lund, T.L. Boyd, Direct utilization of geothermal energy 2015 worldwide review, *Geothermics* 60 (2016) 66–93, <https://doi.org/10.1016/j.geothermics.2015.11.004>.
- [6] C.M. Aiken, Barotropic tides of the Chilean Inland Sea and their sensitivity to basin geometry, *J. Geophys. Res. Ocean.* 113 (2008), <https://doi.org/10.1029/2007JC004593>.
- [7] J. Cruz, M.D. Thomson, E. Stavroulia, Preliminary Site Selection Chilean Marine Energy Resources, 2009.
- [8] S.P. Neill, M.R. Hashemi, M.J. Lewis, The role of tidal asymmetry in characterizing the tidal energy resource of Orkney, *Renew. Energy* 68 (2014) 337–350, <https://doi.org/10.1016/j.renene.2014.01.052>.
- [9] P.E. Robins, S.P. Neill, M.J. Lewis, S.L. Ward, Characterising the spatial and temporal variability of the tidal-stream energy resource over the northwest European shelf seas, *Appl. Energy* 147 (2015) 510–522, <https://doi.org/10.1016/j.apenergy.2015.03.045>.
- [10] Z. Define, K.A. Haas, H.M. Fritz, GIS based multi-criteria assessment of tidal stream power potential: a case study for Georgia, USA, *Renew. Sustain. Energy Rev.* 15 (2011) 2310–2321, <https://doi.org/10.1016/j.rser.2011.02.005>.
- [11] W.B. Chen, W.C. Liu, M.H. Hsu, Modeling assessment of tidal current energy at Kinmen Island, Taiwan, *Renew. Energy* 50 (2013), 10731082, <https://doi.org/10.1016/j.renene.2012.08.080>.
- [12] J.-F. Filipot, C. Delafosse, T. Marzin, S. Baston, On the modeling errors in the tidal power assessment, in: 5th Int. Conf. Ocean Energy, vol. 4, 2014, p. 7. Novemb. 2014, Halifax, Halifax, <http://archimer.ifremer.fr/doc/00230/34114/>.
- [13] C. Frid, E. Andonegi, J. Depestele, A. Judd, D. Rihan, S.I. Rogers, E. Kenchington, The environmental interactions of tidal and wave energy generation devices, *Environ. Impact Assess. Rev.* 32 (2012) 133–139, <https://doi.org/10.1016/j.eiar.2011.06.002>.
- [14] M. De Dominicis, R. OHara Murray, J. Wolf, Multi-scale ocean response to a large tidal stream turbine array, *Renew. Energy* 114 (2017) 1160–1179, <https://doi.org/10.1016/j.renene.2017.07.058>.
- [15] S.P. Neill, E.J. Litt, S.J. Couch, A.G. Davies, The impact of tidal stream turbines on large-scale sediment dynamics, *Renew. Energy* 34 (2009) 2803–2812, <https://doi.org/10.1016/j.renene.2009.06.015>.
- [16] M. Lewis, S.P. Neill, P.E. Robins, M.R. Hashemi, Resource assessment for future generations of tidal-stream energy arrays, *Energy* 83 (2015) 403–415, <https://doi.org/10.1016/j.energy.2015.02.038>.
- [17] M. Cceres, A. Valle-Levinson, L. Atkinson, Observations of cross-channel structure of flow in an energetic tidal channel, *J. Geophys. Res.* 108 (2003) 3114, <https://doi.org/10.1029/2001JC000968>.
- [18] V.H. Marn, F.J. Campuzano, Un Modelo Hidrodinámico-Barotrópico para los Fiordos Australes de Chile entre los 41° S y los 46° S, *Rev. Cienc. Y Tecnol. Del Mar.* 31 (2008) 125–136.
- [19] M. Guerra, R. Cienfuegos, J. Thomson, L. Suarez, Tidal energy resource characterization in Chacao Channel, Chile, *Int. J. Mar. Energy* 20 (2017) 1–16, <https://doi.org/10.1016/j.ijome.2017.11.002>.
- [20] P. Evans, A. Mason-Jones, C. Wilson, C. Wooldridge, T. O'Doherty, D. O'Doherty, Constraints on extractable power from energetic tidal straits, *Renew. Energy* 81 (2015) 707–722, <https://doi.org/10.1016/j.renene.2015.03.085>.
- [21] A.J. Goward Brown, S.P. Neill, M.J. Lewis, Tidal energy extraction in three-dimensional ocean models, *Renew. Energy* 114 (2017), 244257, <https://doi.org/10.1016/j.renene.2017.04.032>.
- [22] S.P. Neill, A. Vgler, A.J. Goward-Brown, S. Baston, M.J. Lewis, P.A. Gillibrand, S. Waldman, D.K. Woolf, The wave and tidal resource of Scotland, *Renew. Energy* 114 (2017) 317, <https://doi.org/10.1016/j.renene.2017.03.027>.
- [23] R. Marsooli, P.M. Orton, G. Mellor, N. Georgas, A.F. Blumberg, A coupled circulation-wave model for numerical simulation of storm tides and waves, *J. Atmos. Ocean. Technol.* 34 (2017) 1449–1467, <https://doi.org/10.1175/JTECH-D-17-0005.1>.
- [24] D.M. Farmer, H.J. Freeland, The physical oceanography of Fjords, *Prog. Oceanogr.* 12 (1983), [https://doi.org/10.1016/0079-6611\(83\)90004-6](https://doi.org/10.1016/0079-6611(83)90004-6).
- [25] D. Soto, F. Norambuena, Evaluation of salmon farming effects on marine systems in the inner seas of southern Chile: a large-scale mensurative experiment, *J. Appl. Ichthyol.* 20 (2004) 493–501, <https://doi.org/10.1111/j.1439-0426.2004.00602.x>.
- [26] C. Molinet, A. Valle-Levinson, C.A. Moreno, M. Cceres, M. Bello, M. Castillo, Effects of sill processes on the distribution of epineustonic competent larvae in a stratified system of Southern Chile, *Mar. Ecol. Prog. Ser.* 324 (2006) 95–104, <https://doi.org/10.3354/meps324095>.
- [27] N. Silva, C.A. Vargas, Hypoxia in Chilean patagonian fjords, *Prog. Oceanogr.* 129 (2014) 62–74, <https://doi.org/10.1016/j.pocean.2014.05.016>.
- [28] G. Olivares, H.H. Seplveda, B. Yannicelli, Definition of sanitary boundaries to prevent ISA spread between salmon farms in southern Chile based on numerical simulations of currents, *Estuar. Coast Shelf Sci.* 158 (2015) 31–39, <https://doi.org/10.1016/j.ecss.2015.02.013>.
- [29] A.H. Buschmann, F. Cabello, K. Young, J. Carvajal, D.A. Varela, L. Henrquez, Salmon aquaculture and coastal ecosystem health in Chile: analysis of regulations, environmental impacts and bioremediation systems, *Ocean Coast Manag.* 52 (2009) 243–249, <https://doi.org/10.1016/j.ocecoaman.2009.03.002>.
- [30] M. Cceres, A. Valle-Levinson, H.H. Seplveda, K. Holderied, Transverse variability of flow and density in a Chilean fjord, in: *Cont. Shelf Res.*, 2002, pp. 1683–1698, [https://doi.org/10.1016/S0278-4343\(02\)00032-8](https://doi.org/10.1016/S0278-4343(02)00032-8).
- [31] A. Valle-Levinson, N. Sarkar, R. Sanay, D. Soto, J. Len, Spatial structure of hydrography and flow in a Chilean fjord, Estuario Reloncav, *Estuaries and Coasts* 30 (2007), 113126, <https://doi.org/10.1007/BF02782972>.
- [32] C. Calvete, M. Sobarzo, Quantification of the surface brackish water layer and frontal zones in southern Chilean fjords between Boca del Guafo (43°30'S) and Estero Elefantes (46°30'S), *Cont. Shelf Res.* 31 (2011) 162–171, <https://doi.org/10.1016/j.csr.2010.09.013>.
- [33] M.I. Castillo, O. Pizarro, U. Cifuentes, N. Ramirez, L. Djurfeldt, Subtidal dynamics in a deep fjord of southern Chile, *Cont. Shelf Res.* 49 (2012) 73–89, <https://doi.org/10.1016/j.csr.2012.09.007>.
- [34] M.I. Castillo, O. Pizarro, N. Ramirez, M. Cceres, Seiche excitation in a highly stratified fjord of southern Chile: the Reloncav fjord, *Ocean Sci.* 13 (2017) 145–160, <https://doi.org/10.5194/os-13-145-2017>.
- [35] H.A. Sievers, N. Silva, Water masses and circulation in austral Chilean channels and fjords, in: *Prog. Oceanogr. Knowl. Chil. Inter. Waters, from Puerto Montt to Cape Horn, Comité Oceanográfico Nacional - Pontificia Universidad Católica de Valparaíso, Valparaíso, 2008*, pp. 53–58.
- [36] N. Silva, A. Valdenegro, Caracterización oceanográfica de canales australes chilenos entre la Boca del Guafo y los Canales Pulluche-Chacabuco (CIMAR 8 fiordos), *Rev. Cienc. Y Tecnol. Del Mar.* 31 (2008) 5–44.
- [37] M. Cceres, A. Valle-Levinson, J. Fierro, C. Valenzuela, M. Castillo, Variabilidad Transversal del Flujo y de la Densidad en la Boca del Fiordo Aysn, *Rev. Cienc. Y Tecnol. Del Mar.* 33 (2010) 5–15.
- [38] M. Cceres, A. Valle-Levinson, Variabilidad transversal del flujo y salinidad en paso Nao, *Rev. Cienc. Y Tecnol. Del Mar.* 33 (2010) 45–58.
- [39] S. Pantoja, J. Luis Iriarte, G. Daneri, Oceanography of the Chilean Patagonia, *Cont. Shelf Res.* 31 (2011) 149–153, <https://doi.org/10.1016/j.csr.2010.10.013>.
- [40] A. Valle-Levinson, M.A. Caceres, O. Pizarro, Variations of tidally driven three-layer residual circulation in fjords, *Ocean Dynam.* 64 (2014) 459–469, <https://doi.org/10.1007/s10236-014-0694-9>.
- [41] J. Letelier, L. Soto-Mardones, S. Salinas, P. Osuna, D. Lpez, H.H. Seplveda, E. Pinilla, C. Rodrigo, Variabilidad del viento, oleaje y corrientes en la región norte de los fiordos Patagónicos de Chile, *Rev. Biol. Mar. Oceanogr.* 46 (2011) 363–377, <https://doi.org/10.4067/S0718-19572011000300007>.
- [42] L. Debreu, P. Marchesiello, P. Penven, G. Cambon, Two-way nesting in split-explicit ocean models: algorithms, implementation and validation, *Ocean Model.* 49–50 (2012) 1–21, <https://doi.org/10.1016/j.ocemod.2012.03.003>.
- [43] A.F. Shchepetkin, J.C. McWilliams, The regional oceanic modeling system (ROMS): a split-explicit, free-surface, topography-following-coordinate oceanic model, *Ocean Model.* 9 (2005) 347–404, <https://doi.org/10.1016/j.ocemod.2004.08.002>.
- [44] A. Arakawa, V.R. Lamb, A potential enstrophy and energy conserving scheme for the shallow water equations, *Mon. Weather Rev.* 109 (1981) 18–36, [https://doi.org/10.1175/1520-0493\(1981\)109<0018:APEAEC;2.0.CO;2](https://doi.org/10.1175/1520-0493(1981)109<0018:APEAEC;2.0.CO;2).
- [45] J.C. Warner, C.R. Sherwood, H.G. Arango, R.P. Signell, Performance of four turbulence closure models implemented using a generic length scale method, *Ocean Model.* 8 (2005) 81–113, <https://doi.org/10.1016/j.ocemod.2003.12.003>.
- [46] D.T. Sandwell, S.T. Gille, W.H.F. Smith, Bathymetry from Space: Oceanography, Geophysics, and Climate, Bethesda, Maryland, 2002. [www.igpp.ucsd.edu/bathymetryworkshop](http://www.igpp.ucsd.edu/bathymetryworkshop).
- [47] D.B. Haidvogel, H.G. Arango, K. Hedstrom, A. Beckmann, P. Malanotte-Rizzoli, A.F. Shchepetkin, Model evaluation experiments in the North Atlantic Basin:

- simulations in nonlinear terrain-following coordinates, *Dyn. Atmos. Oceans* 32 (2000) 239–281, [https://doi.org/10.1016/S0377-0265\(00\)00049-X](https://doi.org/10.1016/S0377-0265(00)00049-X).
- [48] J.I. Antonov, D. Seidov, T.P. Boyer, R.A. Locarnini, A.V. Mishonov, H.E. Garcia, O.K. Baranova, M.M. Zweng, D.R. Johnson, *World Ocean Atlas 2009*, vol. 2, 2010, <https://doi.org/10.1182/blood-2011-06-357442>. Salinity.
- [49] R.A. Locarnini, A.V. Mishonov, J.I. Antonov, T.P. Boyer, H.E. Garcia, O.K. Baranova, M.M. Zweng, D.R. Johnson, *World Ocean Atlas 2009*, vol. 1, 2010, <https://doi.org/10.1182/blood-2011-06-357442>. Temperature.
- [50] G.D. Egbert, S.Y. Erofeeva, Efficient inverse modeling of barotropic ocean tides, *J. Atmos. Ocean. Technol.* 19 (2002) 183–204, [https://doi.org/10.1175/1520-0426\(2002\)019<0183:EIMOBO>2.0.CO;2](https://doi.org/10.1175/1520-0426(2002)019<0183:EIMOBO>2.0.CO;2).
- [51] A. Valle-Levinson, L.P. Atkinson, Spatial gradients in the flow over an estuarine channel, *Estuaries* 22 (1999) 179, <https://doi.org/10.2307/1352975>.
- [52] G. Siedler, U. Paul, Barotropic and baroclinic tidal currents in the eastern basins of the North Atlantic, *J. Geophys. Res. Oceans* 96 (1991) 22259–22271, <https://doi.org/10.1029/91JC02319>.
- [53] R. Pawlowicz, B. Beardsley, S. Lentz, Classical tidal harmonic analysis including werror estimates in MATLAB using T\_TIDE, *Comput. Geosci.* 28 (2002), 929937, [https://doi.org/10.1016/S0098-3004\(02\)00013-4](https://doi.org/10.1016/S0098-3004(02)00013-4).
- [54] R.D. Pingree, D.K. Griffiths, S2 tidal simulations on the north-west European shelf, *J. Mar. Biol. Assoc. U. K.* 61 (1981) 609–616, <https://doi.org/10.1017/S0025315400048074>.
- [55] A. Bahaj, L. Myers, Fundamentals applicable to the utilisation of marine current turbines for energy production, *Renew. Energy* 28 (2003) 2205–2211, [https://doi.org/10.1016/S0960-1481\(03\)00103-4](https://doi.org/10.1016/S0960-1481(03)00103-4).
- [56] N. Senechal, A. Sottolichio, F. Bertrand, L. Goeldner-Gianella, T. Garlan, Observations of waves' impact on currents in a mixed-energy tidal inlet: arcachon on the southern French Atlantic coast, *J. Coast. Res. Special Issue* 65 (2013) 2053–2058, <https://doi.org/10.2112/SI65-347.1>.
- [57] M.R. Hashemi, S.P. Neill, P.E. Robins, A.G. Davies, M.J. Lewis, Effect of waves on the tidal energy resource at a planned tidal stream-array, *Renew. Energy* 75 (2015) 626–639, <https://doi.org/10.1016/j.renene.2014.10.029>.